

Analysis of Dual Bell Nozzle Configurations: Design Parameters and Performance Measurements

T. Chehat^{1,2†}, H. Kbab¹, W. Hamaidia² and B. Benaouda Zouaoui¹

¹ *Aeronautics and Space Studies Institute, Aeronautical Sciences Laboratory, University of Blida 1, Blida, Algeria*

² *Higher School of Aeronautical Techniques, Dar El-Beida, Algiers, Algeria*

† *Corresponding Author Email: CHEHAT.TAHAR@etu.univ-blida.dz*

ABSTRACT

The auto-adaptation capability of the dual-bell nozzle (DBN) facilitates and enhances the performance of rocket propulsion systems, thus rendering it suitable for sea-level operations and efficient transitions at varying altitudes. This study compares the performances of three different types of DBNs in terms of thrust efficiency and altitude compensation. Additionally, a set of simulations is performed to investigate the key design parameters, such as the nozzle geometry, expansion ratio, and contour shapes, to evaluate their effect on the overall performance. After performing an extended literature review of dual-bell propulsion nozzles, the abovementioned parameters are examined systematically to provide deeper insights into their effects on thrust generation and altitude adaptability. The results show that thrust-optimised parabolic base nozzle designs can significantly enhance the thrust efficiency in aeroengines and facilitate adaptation to a wide range of altitudes. This study provides critical insights into the essential design aspects for optimising the performance of DBNs, thus contributing significantly to advancements in rocket propulsion. The obtained results offer valuable guidelines for enhancing nozzle design and accuracy, as well as facilitate efficiency improvement in aerospace applications, thereby ultimately improving the overall effectiveness of propulsion systems.

Article History

Received November 1, 2024

Revised January 27, 2025

Accepted February 11, 2025

Available online May 5, 2025

Keywords:

Dual bell nozzle

CFD

Nozzle design

Rocket propulsion

Altitude compensation

1. INTRODUCTION

Dual-bell nozzles (DBNs) provide an effective option for enhancing efficiency at elevated altitudes while mitigating the potential of dangerous side loads during operations at lower altitudes (Stark & Génin, 2010). Figure 1 illustrates the unique characteristics of DBNs, which exhibit two distinct shapes between the throat and outlet. This design features a foundational contour with a wall inflection that distinguishes it from an extension contour (Verma et al., 2015; Stark et al., 2016). In 1949, a dual-bell nozzle design was introduced, which was subsequently patented by Rocketdyne in the 1960s. Interest in this design has surged because of advancements in computational fluid dynamics, particularly throughout the 1990s. Experiments performed at Rocketdyne and at the European Space Agency validated its viability. The DBN configuration, with angled extensions and consistent pressure, exhibited superior performance during transitions compared with conical and Rao optimum nozzles (Khare & Saha, 2021). A constant-pressure (CP)

extension was selected as the baseline because of its satisfactory transition characteristics and optimal performance at high flight levels. The dual-bell nozzle surpassed the single-bell nozzle in terms of mission analysis (Nürnberger-Genin et al., 2010; Horn & Fisher, 1993). Goel and Jensen conducted a preliminary numerical examination of dual-bell nozzles (Frey & Hagemann, 1995).

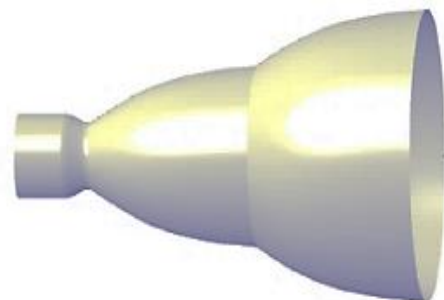


Fig. 1 A typical dual bell nozzle

NOMENCLATURE				
Latin Alphabet				
A	cross section area	$k - \varepsilon$	turbulence model	
V	average velocity	$k - \omega$	turbulence model	
u	velocity components	ε	turbulent dissipation energy	
b	base nozzle	μ	dynamic viscosity	
C_D	aspiration drag coefficient	μ_t	turbulent viscosity	
C_F	thrust coefficient	Subscripts		
C_f	pressure force coefficient	i	spatial index	
C_m	mass coefficient	j	spatial index	
e	extension nozzle	0	stagnation condition	
F	thrust	w	wall	
I_{sp}	specific impulsion	tot	total length	
L	longer	th	throat	
M	Mach number	Abbreviations		
P	pressure	CFD	Computational Fluid Dynamic	
P_a	the ambient pressure is specified for a given NPR.	CP	Constant Pressure	
R	radius	FSS	Free Shock Separation	
T	temperature	SST	Shear stress transport	
X	abscise coordinate	RANS	Reynolds-Averaged Navier-Stokes	
Y	ordinate coordinate	DBN	Dual Bell Nozzle	
x, y	spatial variable	MLN	Minimum Length Nozzle	
Greek Alphabet			TIC	Truncated Ideal Contour
α	inflection angle	TOP	Thrust Optimized Parabola	
θ	half-angle	MLN DBN	dual bell nozzle with minimum length nozzle base nozzle	
ρ	density	TIC DBN	dual bell nozzle with truncated ideal contour base nozzle	
		TOP DBN	dual bell nozzle with thrust optimized parabola base nozzle	

This study comprehensively evaluates dual-bell characteristics to address critical aspects such as contour design, flow-field development, and transition behaviour from startup to higher altitudes. Based on the results of parametric numerical simulations, the DBN contour results in minimal additional performance losses. This report underscores the necessity for further experimental research to deepen our understanding and propose strategies to reduce the flow transition length by adjusting the thrust chamber pressure during controlled shifts in separation points.

In the 2000s, European and American researchers conducted extensive experimental and computational investigations into DBN (Hagemann et al., 1998). Recent studies focused on enhancing the design characteristics of twin-bell nozzles, namely, the optimal shape and length of the expanded section. A comprehensive analysis of the Ariane 5 Evolution Cryotechnique Type A (ECA), which uses twin bell nozzles, was conducted by (Martelli et al., 2007; Stark et al., 2016) analysing various Vulcain 2 extension shapes. Analytical and numerical models predicted a potential payload increase of up to 490 kg in a geostationary transfer orbit. Additionally, a study demonstrated the viability of ‘sea-level transitional DBNs’, which can enhance payload capacity by up to 200 kg and enable mode changes when the engine is initiated at sea level. DBNs offer a simple design, efficient control of flow separation, and reduced weight, despite potential challenges such as performance losses, cooling difficulties, and mechanical complexity. Kbab et al. (2017) further investigated the flow behaviour by

employing the method of characteristics to delineate the profile of a DBN.

Génin et al. (2013a) conducted empirical and computational investigations into a DBN to evaluate the heat-flux distribution. The contour area in the inflection zone demonstrated elevated heat-flow values in two operational modes (high altitude and sea level). In the altitude mode, heat flow increased by approximately 40%. Flow separation in the inflection zone was more prominent during the initial and transient transition periods. Figure 2 illustrates the two modes of a DBN. At sea level, the flow separates at the contour intersection in a regulated and cohesive manner (see Fig. 2. a). The restricted area ratio causes a decrease in the internal load production, although the thrust increases. As the atmospheric pressure decreases with altitude, the nozzle pressure ratio (NPR) increases. Upon reaching the transition NPR, which occurs at a specific altitude, the separation point shifts rapidly from the junction position to the exit of the nozzle, thus resulting in a fully expanded flow through the extension, as shown in Fig. 2. b). Consequently, this higher area ratio increases the thrust.

Schneider and Genin (2016) examined the effects of different turbulence models and changes in feed pressure on the flow-transition properties in DBNs. Improved results were observed when the Spalart–Allmaras (one-equation model) and Reynolds stress models were used. Génin et al. (2013c) examined a planar DBN model under hot- and cold-flow conditions in several tests. An analysis of the shock wave around the wall revealed the

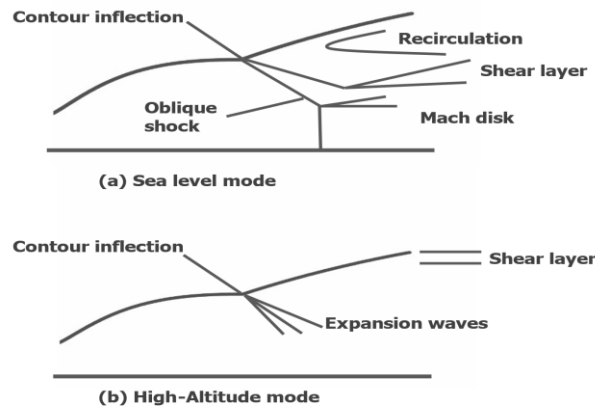


Fig. 2 Exploring DBN Modes: Sea-Level and High-Altitude Configurations

configuration and location of the separation front. In the sea-level mode, both the computational and experimental results were similar. However, for higher NPRs, the expected separation point was indicated upstream of its observed location. Verma et al. (2013) conducted experiments to analyse the effects of various Reynolds numbers on the transition dynamics of DBNs during high-altitude phase simulations within a combustion chamber. Verma et al. (2014) examined the effects of ambient-pressure variations on the transition behaviour of DBNs. Toufik et al. (2016) used the technique of characteristics to investigate the design of DBNs and assessed various factors and performance indicators. Davis et al. (2015) devised a twin-bell nozzle contour design methodology, which was then utilised in nozzles designed for sounding rockets or nanosatellite launchers. Verma et al. (2015) performed cold-gas experiments at sea level utilising a small-scale DBN to examine unstable flow conditions during the transition period. The findings indicated that the primary cause of side-load generation was a highly erratic flow during the transition. Genin et al. (2013c) combined experimental and computational methods to identify the most effective approaches for modifying the transition behaviour by varying the extension geometry. Hagemann et al. (2002) conducted a comprehensive analytical and experimental investigation into the aerodynamic characteristics of different DBNs. Frey and Hagemann (1999) investigated several design factors related to wall inflection and nozzle extension, with emphasis on the effects of different extension types on transition behaviour. They identified two key forms of nozzle extension: positive-pressure and CP extensions, which can generate abrupt flow changes. Genin et al. (2012) employed computational methods to investigate the flow dynamics within a DBN, with emphasis on comparing two operational modes and the switch between them as the NPR values varied.

Khare and Saha (2021) investigated sea-level transitioning twin-bell nozzles for the Ariane 5 ECA. In particular, they examined the distinct geometries of Vulcain 2 and Vulcain 2.1 nozzle extensions, with emphasis on the positioning of the inflection point and the maintenance of a uniform wall pressure. The verified analytical approach utilised for these parameters

forecasted the effect of the twin-bell nozzles on the payload mass transported to the geostationary transfer orbit. They focused on enhancing the nozzle design to increase the payload-delivery efficiency. Stark et al. (2019) examined the advancement of a film-cooled DBN incorporated into a pre-existing LOX/GH₂ thrust-chamber assembly. The reduced DBN employed gaseous hydrogen for cooling-film injection and was derived from a previously evaluated film-cooled truncated ideal contour (TIC) nozzle. Investigations into hot flows will be performed at the P8 facility to examine the effect of fluctuations in the cooling-film mass flow and regeneration outer flow on the mode transition of the DBN. A uniform heat flow and cooling-film distribution were achieved under sea-level test conditions through comprehensive computer studies and design modifications. Hamitouche et al. (2019) utilised a numerical approach that combined the direct method for the second bell using the method of characteristics for the first bell. Their results showed consistent performance and differing dimensions when compared with experimental data obtained from ONERA-France and CNRS-Orleans. Verma et al. (2020) examined the flow dynamics within a DBN by comparing scenarios with and without film cooling. Léger et al. (2020) examined the utilisation of secondary radial injections to regulate the changeover of flow regimes. The results indicated that, even at minimal mass flow rates, the technique may substantially postpone both the transition and retransition processes, thus aligning them closer to the ideal transition point. Moreover, their experimental findings indicated a significant decrease in the side loads or their complete eradication. Scharnowski and Kähler (2021) examined the afterbody flow of a conventional space launcher, which highlighted the interaction between the engine's exhaust jet and the separated shear layer during the ascent of the rocket through the atmosphere. The findings showed that the reattachment length decreased as the nozzle pressure ratio increased. Researchers at the EDITH nozzle test laboratory in Orléans, France conducted studies on an axisymmetric DBN and showed that secondary fluidic injection significantly affected flow-regime transitions, thus enhancing propulsive performance (Léger et al., 2021). Cimini et al. (2021) simulated a cold-gas DBN

under high-Reynolds-number conditions at sea level, which indicated controlled separation and minimal aerodynamic side loads. The nozzle wall pressure indicated a continuous tone associated with symmetric shock movement, accompanied by a low side-load magnitude that aligned with experimental findings. Liu and Li (2023) examined the effects of design factors on the aspiration drag of DBNs at various flight altitudes. The findings showed that the aspiration drag decreased consistently in nozzles featuring negative wall-pressure gradient extensions, whereas it began to decline in nozzles with zero- and positive-gradient extensions. Recently, a DBN developed for altitude adaptation during space launches was analysed numerically in various modes. We juxtaposed the numerical results with experimental data to analyse the flow behaviour and observed hysteretic phenomena at the inflection points when the nozzle pressure ratio increased (Wu et al., 2023).

The present study investigates a DBN design to improve the efficiency-related thrust and transition behaviour at various altitudes via computational simulations. The goal of this study is to identify the optimal geometrical arrangements that minimise performance losses and side loads while enhancing adaptability at different altitudes. This shall be achieved by examining various first-bell profiles, such as TIC, TOP, and MNL, which are associated with a CP expansion of the second-bell shape.

2. DESIGN PROCESS OF DBN

The DBN base design employs the TIC, thrust-optimised parabolic (TOP), or minimum-length nozzle (MLN) configuration. This study evaluated all three configurations to ascertain the one that performed optimally at sea level. DBN extensions should efficiently transition from sea-level to high-altitude operations.

Investigations by Génin et al. (2013b), Verma et al. (2010), and Hagemann et al. (2002) revealed that extensions with CP or positive wall pressures facilitated transitions between modes at significantly shorter timescales. In this study, a fixed wall pressure extension was selected. Base nozzles with CP extensions were fabricated using an improved method of characteristics that was modified to accommodate DBNs with different properties. This design approach utilises the reverse calculation of extension contours, as developed by Yazhou et al. (2022) and Hamitouche et al. (2019), and provides a systematic method for contour design that considers the wall-pressure distribution.

The parameters included the normalised base nozzle length (L_b/R_{th}), expansion ratio (ϵ_e), normalised extension length (L_e/R_{th}), and the half-angles of the base nozzle exit (θ_b) and extension exit (θ_e). For the nozzles, the inflection angle (α), which defines the transition between the base and extension, was provided for the three nozzle configurations (see Fig. 3).

The geometric representations of the DBNs evaluated in this study are illustrated in Figs. 4, 5, and 6. These profiles show DBNs with distinct base contour designs: TIC, MLN, and TOP. The data for each nozzle

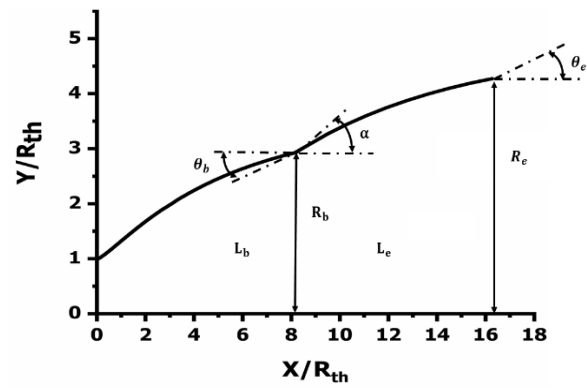


Fig. 3 DBN geometrical parameter

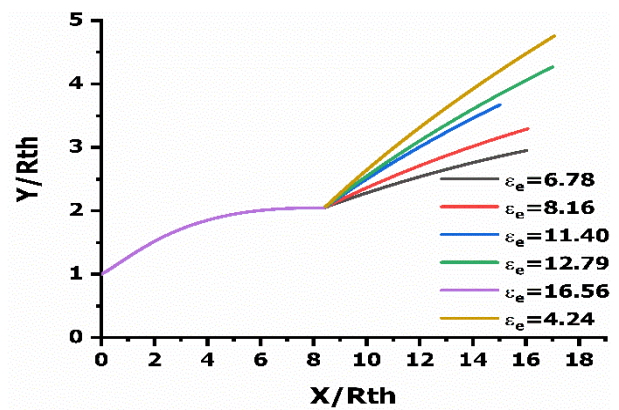


Fig. 4 Exploring area ratio extensions in MLN DBN

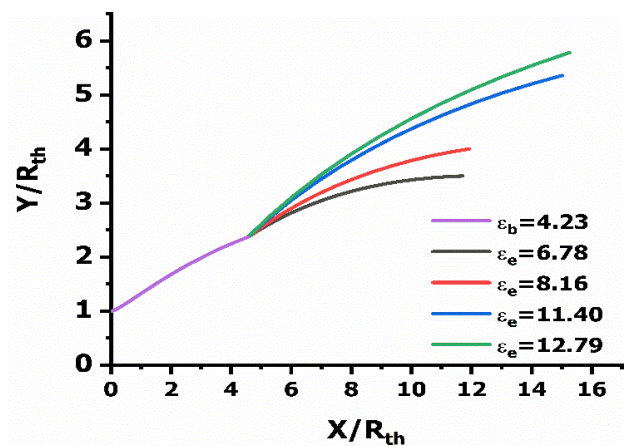


Fig. 5 Exploring area ratio extensions in TIC DBN

configuration are shown under various expansion ratios (ϵ_e) to demonstrate the effect of the latter on the nozzle geometry.

Figure 5 shows DBNs designed using an MLN. The base nozzle was rendered compact by implementing a constant base length (L_b), whereas the extension sections were varied based on ϵ_e , which ranged from 4.23 to 16.56. The geometries showed the manner by which the base nozzle remained compact while the extension length increased with ϵ_e .

Table 1 Geometric Characteristics of DBNs

DBN		L_b/R_{th}	ϵ_b	L_e/R_{th}	ϵ_e	θ_b (°)	α (°)	θ_e (°)
TIC DBN	TIC01	4.55	4.23	7.46	6.78	11.55	7.2	0.82
	TIC02	4.55	4.23	7.68	8.16	11.55	7.2	4.89
	TIC03	4.55	4.23	10.77	11.40	11.55	7.2	8.29
	TIC04	4.55	4.23	11.01	12.79	11.55	7.2	10.33
	TIC06	8.14	6.78	9.41	11.40	5.90	7.2	2.92
	TIC07	8.14	6.78	9.49	12.79	5.90	7.2	4.86
	TIC08	8.14	6.78	9.54	16.56	5.90	7.2	8.89
	MLN DBN	MLN01	8.37	4.23	11.78	6.78	0.00	7.2
MLN02		8.37	4.23	11.82	8.16	0.00	7.2	7.09
MLN03		8.37	4.23	10.77	11.40	0.00	7.2	11.62
MLN04		8.37	4.23	12.77	12.79	0.00	7.2	11.77
MLN05		8.37	4.23	12.83	16.56	0.00	7.2	14.63
MLN06		12.04	6.78	17.26	11.40	0.00	7.2	4.48
MLN07		12.04	6.78	17.24	12.79	0.00	7.2	5.64
MLN08		12.04	6.78	17.22	16.56	0.00	7.2	8.26
TOP DBN	TOP01	6.39	4.23	10.8	6.78	6.74	7.2	4.26
	TOP02	6.39	4.23	10.8	8.16	6.74	7.2	6.43
	TOP03	6.39	4.23	10.79	11.40	6.74	7.2	10.32
	TOP04	6.39	4.23	10.85	12.79	6.74	7.2	11.59
	TOP05	6.39	4.23	10.83	16.56	6.74	7.2	14.5
	TOP06	9.48	6.78	11.24	11.40	5.53	7.2	5.51
	TOP07	9.48	6.78	11.26	12.79	5.53	7.2	6.73
	TOP08	9.48	6.78	11.24	16.56	5.53	7.2	9.46

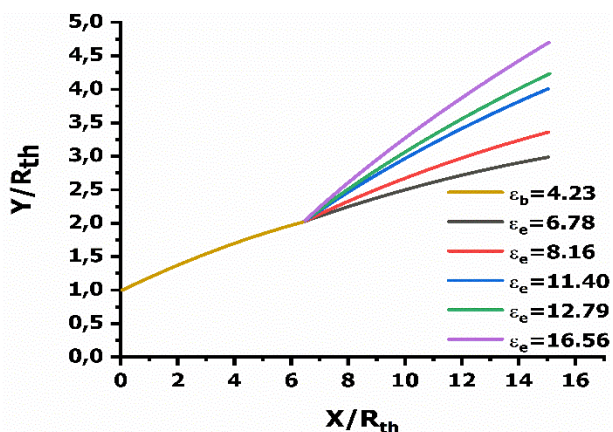


Fig. 6 Exploring area ratio extensions in TOP DBN

The DBNs with a TOP base are shown in Fig. 6. The L_b remained constant in all the configurations, whereas the extension length (L_e) increased as the ϵ_e increased from 4.23 to 16.56. The fundamental geometric characteristics of DBNs are presented in Table 1.

The nozzle geometry was varied while a constant ϵ_e was maintained in all the configurations. The base nozzles with TIC, MLN, and TOP designs had different L_b , L_e and exit half-angles, although they shared the same inflection angle. The ϵ_e values were determined based on the parameter-dependent relationships of the complete nozzle contours.

The parameter names and values were consolidated to enhance the clarity of future presentations. For instance, ‘TIC DBN’ denotes a DBN featuring a TIC base, along with a CP extension at the corresponding ϵ_e .

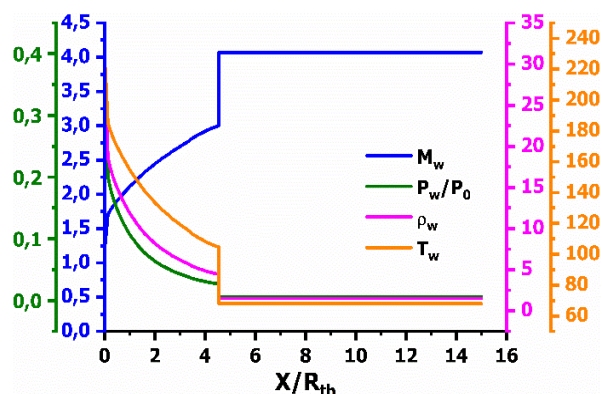


Fig. 7 Wall Parameter Dynamics in TIC DBN

2.1. Examination of flow-parameter variation around DBN wall

The variations in the key flow parameters along the DBN wall for the TIC, MLN, and TOP designs are illustrated in Figs. 7, 8, and 9, respectively. The parameters included the Mach number (M_w), pressure ratio (P_w/P_0), density (ρ_w), and temperature (T_w) at the wall. In both designs, the second stage operated consistently under a CP transition, thus ensuring a smooth shift from sea-level to high-altitude operation.

Figure 7 illustrates the evolution of the flow parameters along the TIC DBN wall with a CP extension. The M_w gradually along the nozzle length, with a significant rise position $X/R_{th} = 5$, thus denoting the start of the extension.

This transition from the base nozzle to the second extension signifies the auto-adaptation of the nozzle for

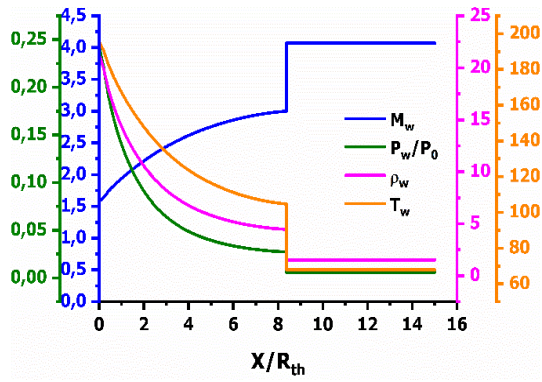


Fig. 8 Wall Parameter Dynamics in MLN DBN

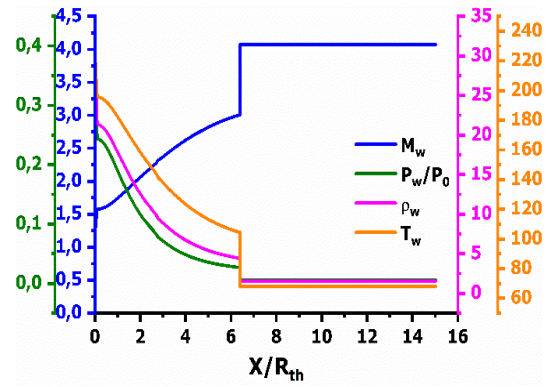


Fig. 9 Wall Parameter Dynamics in TOP DBN

high-altitude operations. In the second bell, the flow was stabilised at a CP.

The P_w/P_0 decreased rapidly as gas expanded in the primary bell, followed by a significant decrease near the inflection point. The second bell sustained the optimal wall pressure, thereby ensuring efficient performance. The T_w had most likely decreased monotonously and saturated in the final section of the nozzle extension, thus corresponding to an adiabatic operation under CP in the second bell.

The evolution of the flow parameters for the MLN DBN is illustrated in Fig. 8. Under these conditions, the CP extension yielded the following results: The M_w increased rapidly at approximately $X/R_{th} = 8$, whereas the continuous-pressure extension stabilised the flow in the second-bell region. The P_w/P_0 diminished progressively in the base section; however, it declined more significantly than the TIC DBN. At the inflection point, no alterations occurred until the second bell became stable. However, if the present altitude or greater is attained, then all the other parameters must be maintained. The ρ_w decreased uniformly over the nozzle length. In the second bell, the continuous-pressure extension was maintained at a stable density. The T_w exhibited a similar pattern, i.e. it decreased equally throughout the injection lines and subsequently stabilised within the second bells. This demonstrates efficient thermal management under a CP.

Figure 9 shows that the TOP DBN with a CP extension altered the flow-parameter evolution. The parabolic shape of the TOP base indicates a slightly more gradual increase in the M_w compared with designs such as the TIC or MLN DBN. At the junction point, the Mach number decreased abruptly (thus forming an expansion fan) until it reached the imposed value in the second bell. The P_w/P_0 remained evenly distributed along the nozzle length, thus indicating that the pressure decreased gradually. However, after the inflection point, the CP extension guaranteed a uniform wall pressure in the second bell. The ρ_w decreased smoothly along the nozzle, and no abrupt changes in the concentration were observed. In the second bell, the CP extension ensured a stable density. Similar to the other designs, the T_w decreased steadily. However, the parabolic shape of the TOP nozzle and the CP extension resulted in a smooth and uniform temperature distribution.

In all the three nozzle designs (TIC, MLN, and TOP), several key trends were observed, particularly under the influence of the CP extension.

The M_w increased significantly as the flow transitioned from sea level to high altitude. Each nozzle exhibited distinct acceleration profiles; however, the CP extension stabilised the flow in the second bell, thus preventing further pressure drops.

The P_w/P_0 and ρ_w decreased along the nozzle, thus reflecting the ongoing expansion of the exhaust gases. The CP extension ensured that these parameters remained stable in the second bell, thereby providing a smooth transition to high-altitude performance.

The T_w decreased uniformly for all designs and stabilised under CP conditions in the second bell. This indicates effective thermal regulation under the three nozzle geometries.

These flow-parameter evolutions highlight the performance characteristics of each DBN design with a CP extension, thereby providing essential insights for further performance evaluations in various altitude regimes.

2.2. Comparative Analysis of DBN Configurations

To evaluate the performance of the three configurations, i.e. TIC DBN, MLN DBN, and TOP DBN, certain parameters were maintained constant while others were varied. This study independently constrained the force coefficient (C_f), mass coefficient (C_m), and total length (L_{tot}/R_{th}) to systematically evaluate the performance of individual nozzles.

The following formula provides C_f and C_m for N points on the wall:

$$C_f = \sum_{j=1}^{N-1} \left(\frac{P_j}{P_0} \right) \left[\left(\frac{y_{j+1}}{R_{th}} \right)^2 - \left(\frac{y_j}{R_{th}} \right)^2 \right] \quad (1)$$

$$C_m = \sum_{j=1}^{N-1} \sqrt{\left(\frac{x_{j+1}}{R_{th}} - \frac{x_j}{R_{th}} \right)^2 + \left(\frac{y_{j+1}}{R_{th}} - \frac{y_j}{R_{th}} \right)^2} \left(\frac{y_{j+1}}{R_{th}} + \frac{y_j}{R_{th}} \right) \quad (2)$$

The results are presented in Figs. 10 and 11 and Table 2, respectively.

The TIC DBN exhibited the shortest L_{tot}/R_{th} ratio of 4.54 and the lowest C_m value of 19.23, with a fixed C_f of

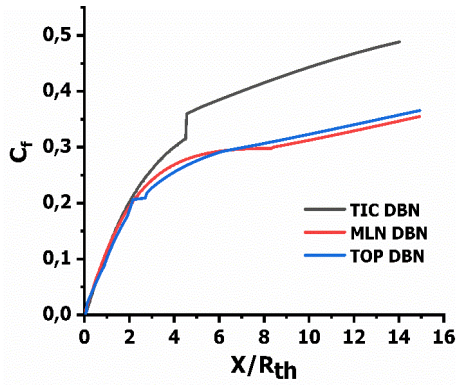


Fig. 10. Evolution of force coefficient along DBN

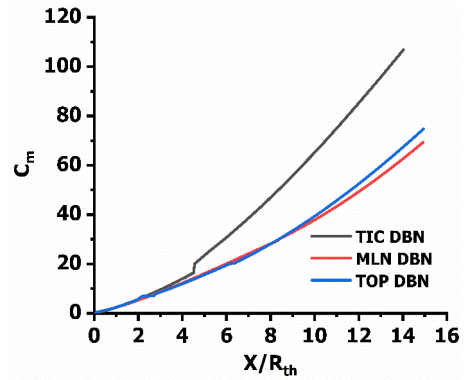


Fig. 11 Evolution of mass coefficient along DBN

Table 2 Geometric and aerodynamic comparison parameters of DBNs

Case	DBN	C _f	C _m	L _{tot} /R _{th}
Fixed C _f	TIC	0.350	19.23	4.54
	MLN	0.350	65.23	14.36
	TOP	0.350	60.62	13.12
Fixed C _m	TIC	0.435	60.00	9.45
	MLN	0.343	60.00	13.62
	TOP	0.349	60.00	13.04
Fixed L _{tot} /R _{th}	TIC	0.488	106.87	15.00
	MLN	0.354	69.30	15.00
	TOP	0.365	74.74	15.00

0.350. The MLN DBN was heavier and extended, whereas the TOP DBN offered a balanced configuration with C_m = 60.62 and L_{tot}/R_{th} = 13.12.

Despite its reduced length, the TIC DBN demonstrated significant side loads, which is attributable to C_m = 60.00. The side loads decreased as the length increased to Cf = 0.343 for the MLN DBN and to Cf = 0.349 for the TOP DBN. At a total length of (L_{tot}/R_{th} = 15.0), the TIC DBN was the most substantial model (mass coefficient, C_m = 106.87) and exhibited the highest force coefficient (Cf = 0.488). Additional examples included the MLN DBN and TOP DBN, which exhibited superior equilibrium for weights and side loads.

The results in Figs. 8 and 9, along with the data in Table 2, indicate that the MLN DBN demonstrated an optimal balance of the C_m relative to the side loads in all the scenarios investigated. The TIC DBN featured the shortest nozzle and, in certain instances, the highest side loads.

3. COMPUTATIONAL APPROACH

The governing equations for a steady compressible turbulent flow based on several turbulence models, as explained in the ANSYS Fluent Theory Guide (2021), are written as follows:

The conservation of mass is expressed as

$$\frac{\partial \rho}{\partial t} + \frac{\partial(\rho u_j)}{\partial x_j} = 0 \quad (3)$$

The conservation of momentum equations is expressed as

$$\frac{\partial(\rho u_i)}{\partial t} + \frac{\partial(\rho u_i u_j)}{\partial x_j} = \frac{\partial[-(P + \frac{2}{3}\rho k)\delta_{ij} + \tau_{ij}]}{\partial x_j} \quad (4)$$

The conservation of total energy is expressed as

$$\frac{\partial(E_t)}{\partial t} + \frac{\partial[(E_t + P)u_j]}{\partial x_j} = \frac{\partial q_j}{\partial x_j} + \frac{\partial(u_j \tau_{ij})}{\partial x_i} - \frac{\partial}{\partial x_j} [\sum_{s=1}^{n_s} h_s J_{sj}] \quad (5)$$

3.1. Computational-Domain Setup

In this study, two-dimensional axisymmetric steady-state simulations were performed to investigate the flow behaviour in DBNs at various altitudes. The simulation domain measured 400R_{th} and 200R_{th} in the x- and y-directions, respectively, as illustrated in Fig. 12. The computational grid ensures a non-dimensional wall distance of y⁺ < 1, which is essential for resolving the efficiency of the viscous boundary layer. The nozzle inlet was specified with a pressure-inlet boundary condition, with a total pressure of stagnation (P₀) of 5.0 MPa and a temperature (T₀) of 293.15 K. The pressure and temperature at the pressure-outlet boundary of the simulation domain were adjusted to replicate the varying ambient conditions encountered at various altitudes.

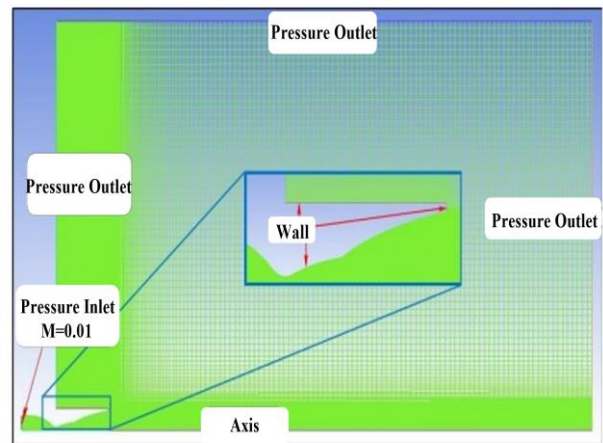


Fig. 12 Simulation Domain, Boundary Conditions, and Nozzle Grid Configuration

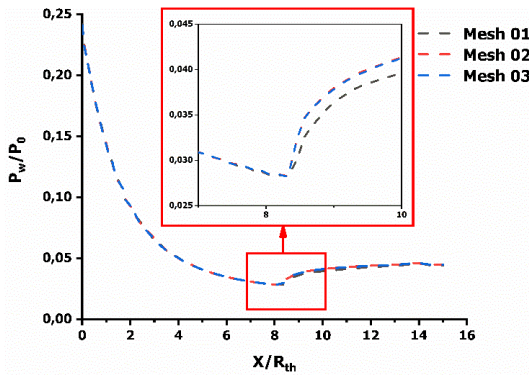


Fig. 13 Pressure profiles on the nozzle wall across three grid configurations

Table 3 Summary of the used grids

Mesh	Coarse	Medium	Fine
Grids Points	601500	753000	868750

3.2. Mesh-Independence Study

To analyse the mesh independence, three resolutions were employed: a coarse mesh with 601500 nodes, a medium mesh with 753000 nodes, and a fine mesh with 868750 nodes (as shown in Table 3). The optimal accuracy of each computational model was determined by analysing the pressure variations along the DBN wall using various mesh configurations, as shown in Fig. 13. Grids 2 and 3 were indistinguishable from one another. This implies that the medium grid, which contains 753,000 nodes, is adequate for the remaining task simulations.

4. RESULTS AND INTERPRETATIONS

4.1. Model Validation

To validate the present numerical method, the experiment of Génin et al. (2013a) was used as a reference. The DBN was designed to operate under a P_0 and T_0 of 2.98 MPa and 293.15 K, respectively. Notably, these conditions were used in computer simulations using the ANSYS Fluent software.

Several different turbulence models have been used to normalise the pressure distribution along the walls of the DBN. The SST $k-\omega$ turbulence model used in this study yielded results that were consistent with the experimental results of Génin et al. (2013b).

Therefore, to enhance our understanding regarding the flow dynamics in a DBN, the SST $k-\omega$ model will be used in future numerical simulations.

The transport equations for k and ω are as follows:

$$\frac{\partial(\rho k)}{\partial t} + \frac{\partial(\rho u_j k)}{\partial x_j} = P - C_\mu \rho \omega k + \frac{\partial \left[\left(\mu + \frac{u_t}{\sigma_k} \right) \frac{\partial k}{\partial x_j} \right]}{\partial x_j} \quad (6)$$

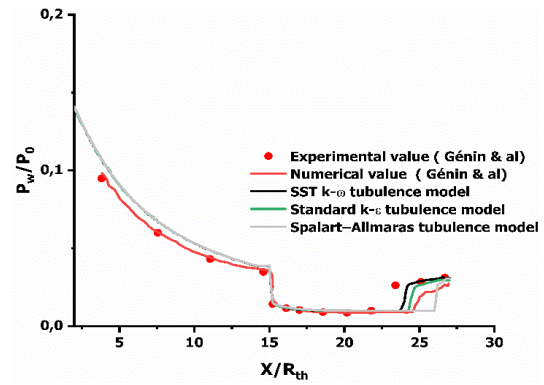


Fig. 14 Pressure Distribution Comparison on the Dual-Bell Nozzle Wall: CFD Results vs. Experimental Data

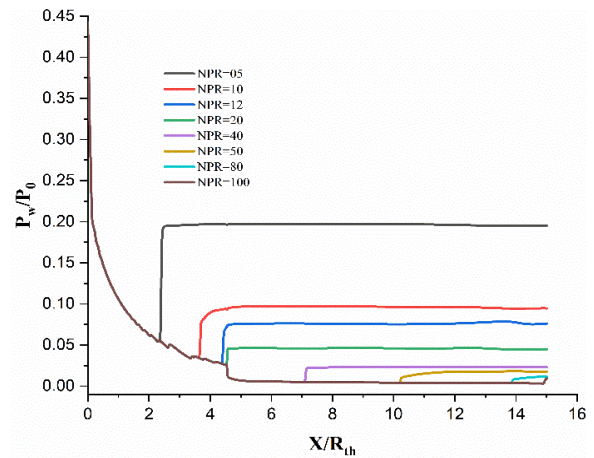


Fig. 15 Pressure profiles along the TIC DBN nozzle wall across various NPRs

$$\frac{\partial(\rho \omega)}{\partial t} + \frac{\partial(\rho u_j \omega)}{\partial x_j} = \frac{\gamma \rho}{\mu_t} P - \beta \rho \omega^2 + \frac{\partial \left[\left(\mu + \frac{u_t}{\sigma_\omega} \right) \frac{\partial \omega}{\partial x_j} \right]}{\partial x_j} + (1 - F_1) \rho \sigma_\omega \frac{1}{\omega} \frac{\partial k}{\partial x_j} \frac{\partial \omega}{\partial x_j} \quad (7)$$

4.2. NPR effects

DBNs depend significantly on the NPR, with rapidly expanding nozzles transitioning swiftly among different operational modes. Each mode, such as the sea-level, sneak-transition, and high-altitude mode, is characterised by unique flow separation behaviours, shock wave configurations, pressure distributions, and Mach-number distributions. The current analysis focuses on the effects of different NPRs on the performance of DBNs.

A- Sea-Level Mode Performance (NPR = 5 to 10)

In this study, strong shock structures and flow separation were observed at low NPRs during sea-level nozzle mode operation. Results of CFD simulations indicated that normal and oblique shock waves originated near the nozzle throat (see Figs. 15, 17, and 19) and propagated downstream along the base nozzle. However, flow separation occurred immediately after these shocks. Figures 15, 17, and 19 illustrate the significant decrease in the nozzle wall pressure from the throat to the exit,

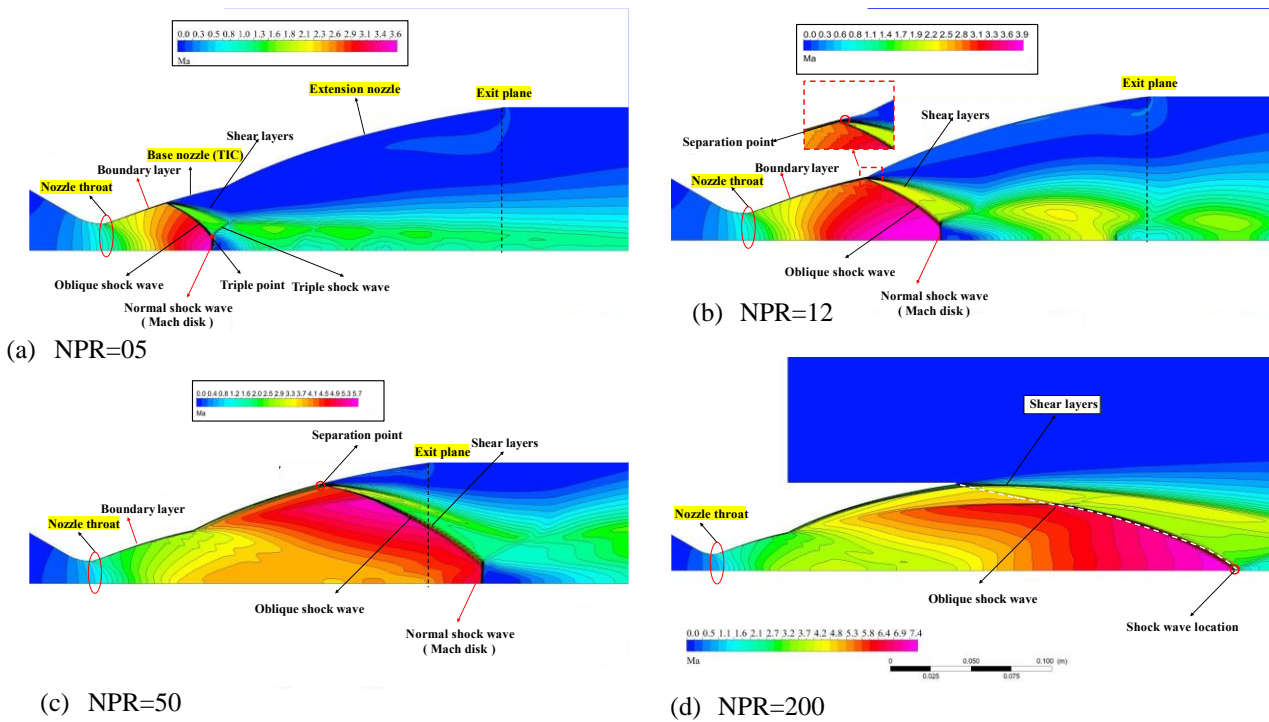


Fig. 16 Detailed illustration of inflection point in Mach number contours across various NPRs (TIC DBN)

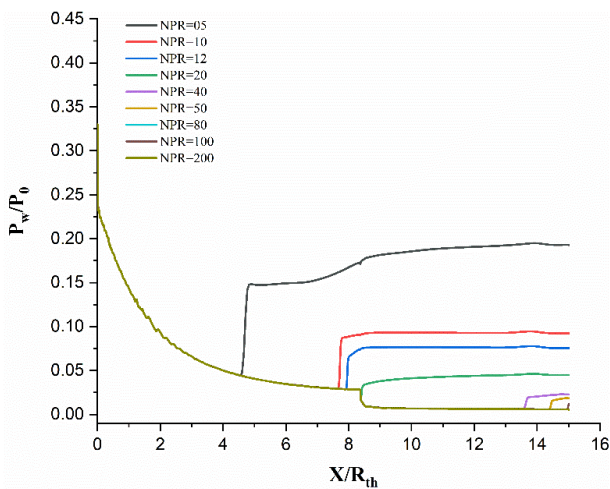


Fig. 17 Pressure profiles along the MLN DBN nozzle wall across various NPRs

accompanied by the well-established free shock separation (FSS) (Hamaidia et al., 2019). This resulted in a thick boundary layer and significant flow disruptions, which ultimately reduced the thrust efficiency.

The shock wave structure was more pronounced in the TIC DBN, which resulted in greater flow instability compared with the cases of the MLN DBN and TOP DBN. Additionally, the Mach number contours presented in Figs. 16, 18, and 20 revealed an abrupt decline at the inflection point, which exacerbated flow separation. Although FSS allows for some degree of expansion, the extensive separation zone resulted in the lower efficiency of the nozzles at sea level.

B- Examination of Transition Modes with NPR Values from 12 to 20

For intermediate NPRs (NPR = 12), the DBN underwent a sneak transition, as illustrated in Figs. 16b, 18b, and 20b. During this phase, the flow transitioned from a low-altitude to a high-altitude operation. Beyond this point, the shock-wave structures became less distinct, with observations varying based on the downstream location of the flow separation point and extending further along the nozzle extension. The FSS at NPR = 12 exhibited a separation point closer to the nozzle exit compared with the case of the TIC DBN, thus indicating a more rapid transition in this regime for the TOP configuration. This resulted in a more stable pressure distribution (Fig. 20b) that was affected less by shock disturbances, thereby enabling a more systematic mode transition.

The TOP nozzle experienced reduced flow disturbances and improved flow attachment compared with the TIC nozzle, which enhanced the thrust performance during the transition.

The transition in the MLN configuration was smooth; however, the exit location shifted further upstream compared with the case of the TOP nozzle. Both the Mach number and pressure distribution indicated a smoother flow transition in the MLN design. Nevertheless, the thrust efficiency remained equivalent within the intermediate NPR range.

C- Analysis of High-Altitude Mode Performance

The DBN reached its high-altitude mode at elevated NPRs, at which point the fully attached flow transitioned to the wall and the shock waves dissipated. At higher NPRs (NPR = 50 and beyond), the corresponding CFD

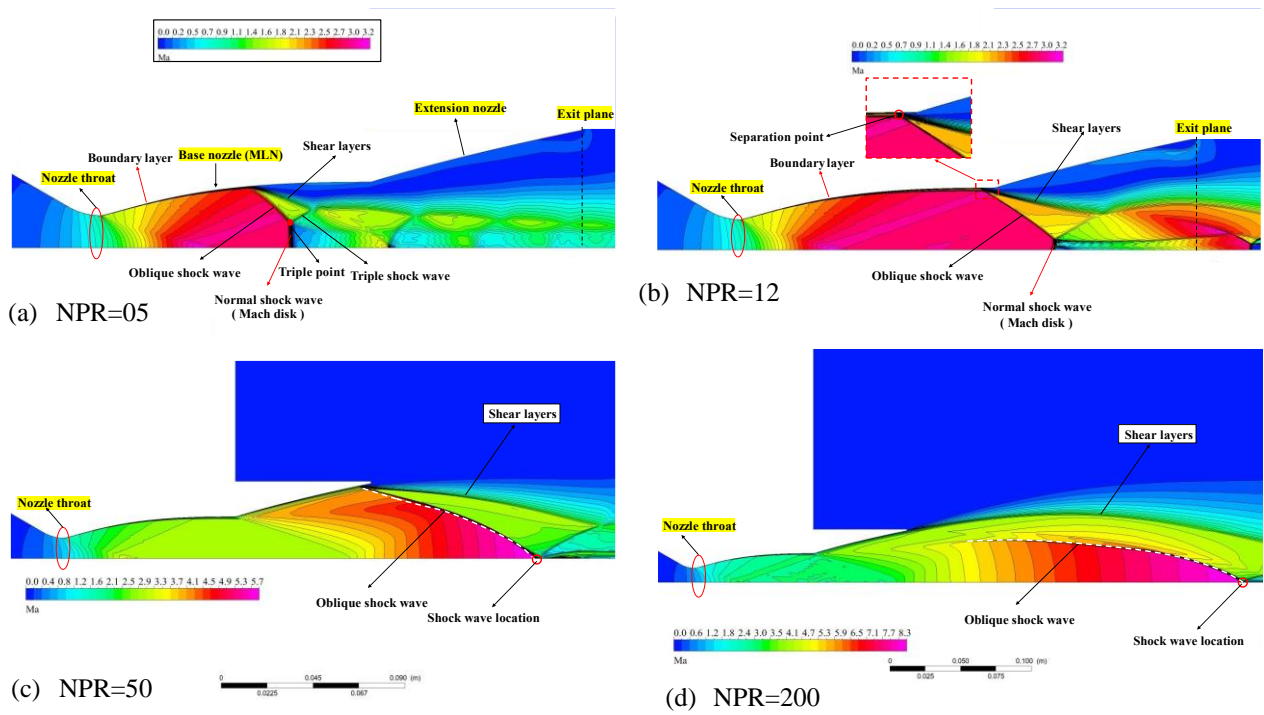


Fig. 18 Detailed illustration of an inflection point in Mach number contours across various NPRs (MLN DBN)

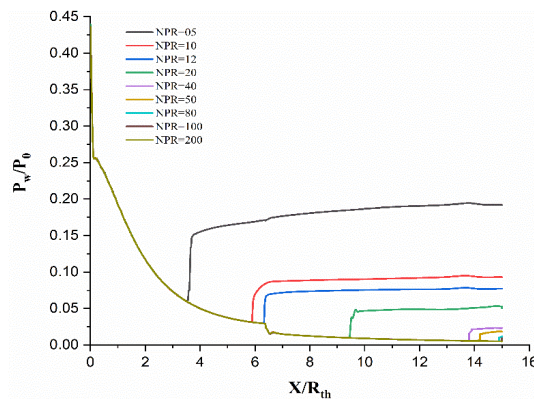


Fig. 19 Pressure profiles along the TOP DBN nozzle wall across various NPRs

findings indicated significantly improved flow behaviour. As the shock-wave structures diminished, the flow stability increased along the second bell, thus resulting in enhanced performance (see Figs. 16d, 18d, and 20d).

In the TOP nozzle, the Mach number increased rapidly, thus resulting in a supersonic flow regime characterised by smooth transitions in the pressure distribution along the nozzle wall (Fig. 19). Figure 20d shows the performance of the TOP design at NPR = 200, where a fully connected flow with minimal pressure variations was achieved under near-vacuum conditions. This configuration yielded the highest thrust efficiency among the three nozzle designs because the flow remained attached and streamlined throughout.

Nozzle-flow attachment occurred later in the TIC design, whose high-altitude performance was superior to that of the TOP nozzle. At elevated altitudes, the MLN

design showed limited performance in terms of high-altitude thrust and minimal shock impact in the attached flow configuration. However, its overall efficiency during mode operation remained inferior at comparable NPR levels when compared to that of the TOP nozzle.

4.3. Comparative Analysis of DBN Configurations

The TIC, MLN, and TOP designs exhibited distinct performance characteristics across a wide range of NPRs, as demonstrated via CFD simulations. As the NPR decreased, the TIC nozzle experienced increased flow turbulence and abrupt shockwave formation, thus resulting in greater thrust losses (Fig. 16). The MLN nozzle offered a balanced performance and excelled at intermediate NPRs, although it did not outperform the TOP nozzle at higher NPRs (see Figs. 18 and 20).

The TOP nozzle consistently demonstrated superior performance at all NPRs. At NPR = 12, it transitioned

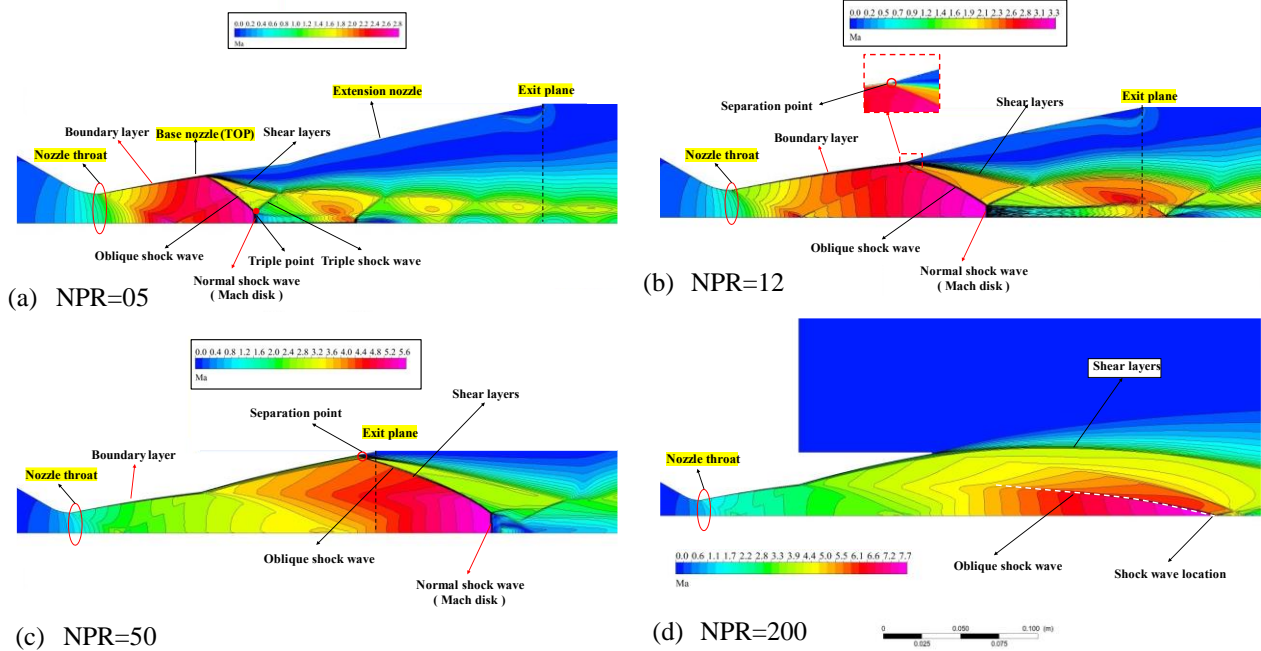


Fig. 20 Detailed illustration of an inflection point in Mach number contours across various NPRs (TOP DBN)

from sea-level to high-altitude mode more rapidly and with less flow separation, thereby enhancing flow adhesion and minimising disruptions. At high altitudes (NPR = 200), the TOP nozzle achieved optimal thrust efficiency, as characterised by stable Mach numbers and pressure distributions, thus rendering it the most effective design for altitude adaptation (Fig. 20).

The CFD simulations indicated that the NPR is critical for determining the operational mode and performance characteristics of a DBN. The transition from startup to operating altitude involves notable variations in the flow separation shock-wave structures and thrust efficiencies.

Notably, the TOP nozzle consistently outperformed all the tested configurations at all NPRs, particularly in terms of the flow transition speed, thrust efficiency, and adherence to high-altitude operational requirements. These results suggest that the TOP nozzle is the optimal advanced DBN configuration for aerospace applications.

4.4. Quantification of Thrust

The thrust F generated by the nozzle can be articulated using many widely recognised performance criteria within the propulsion sector, as follows:

$$F = (\dot{m}v_e + P_e A_e) - P_a A_e = C_F P_c A_t = \dot{m} I_{sp} \quad (8)$$

where \dot{m} is the engine mass-flow rate; C_F denotes the thrust coefficient (dimensionless); I_{sp} denotes the specific impulse [m/s]; v_e and P_e represent the mean values of velocity and pressure at the nozzle exit, respectively; C_F is the amplification of thrust resulting from gas expansion in the rocket nozzle, in contrast to the thrust that would be generated by the chamber pressure exerting on the throat region; and I_{sp} quantifies the efficiency at which a specific

propellant flow rate is converted into thrust (Östlund, 2002).

Specific impulses can be expressed as follows:

$$I_{sp} = \frac{F}{\dot{m}g_0} \quad (9)$$

where I_{sp} is the specific impulse [s] and g_0 is the standard gravitational acceleration (9.81 m/s^2).

Table 4 presents the quantification of thrust for the three DBN designs at various NPRs. This table quantifies the key propulsion parameters, including the specific impulse (I_{sp}) measured in meters per second and seconds, as well as the thrust coefficient (C_F). These parameters provide insights into how efficiently and effectively each nozzle converts the propellant into thrust.

The I_{sp} measures the velocity of exhaust gases exiting the nozzle; a higher I_{sp} indicates more efficient gas acceleration, thus resulting in a greater thrust for a specified amount of propellant consumed per second. The TOP DBN consistently demonstrated higher I_{sp} values at all NPRs, peaking at 673.26 m/s (68.63 s). This highlights its superior propellant efficiency, particularly in the adapted regimes. However, the C_F , which measures the efficacy of gas expansion converting into thrust, shows that TOP DBN was the best for improving thruster performance, as indicated by its C_F of 0.97 at NPR = 5 and 1.59 in NPR 200.

At low NPRs, the TOP DBN exhibited the maximum I_{sp} and C_F , which implies that it is an effective option for thrust generation under atmospheric conditions. As the NPR increased, TOP DBN's performance improved, i.e. its I_{sp} increased by 580.32 m/s and its $C_F = 1.37$ at NPR = 50. By contrast, the TIC DBN exhibited worse high-offset

Table 4 Quantification of the thrust of DBNs with various NPRs

NPRs	TIC DBN			MLN DBN			TOP DBN		
	I_{sp} [m/s]	I_{sp} [s]	C_F	I_{sp} [m/s]	I_{sp} [s]	C_F	I_{sp} [m/s]	I_{sp} [s]	C_F
05	372.81	38.00	0.88	340.65	34.72	0.81	408.40	41.64	0.97
10	468.62	47.77	1.09	482.97	49.23	1.14	494.87	50.45	1.16
12	480.43	48.97	1.12	512.42	52.23	1.20	516.74	52.67	1.21
20	555.60	56.63	1.30	568.94	57.99	1.34	517.37	52.74	1.22
40	571.69	58.27	1.34	575.55	58.67	1.36	553.76	56.45	1.30
50	546.35	55.69	1.28	593.62	60.51	1.40	580.32	59.16	1.37
80	577.16	58.83	1.35	631.31	64.35	1.49	622.90	63.50	1.47
100	598.00	60.96	1.41	645.029	65.75	1.52	638.77	65.11	1.51
200	657.94	67.07	1.55	672.60	68.56	1.59	673.26	68.63	1.59

data performance, which is not depicted in Table 4. However, the TOP DBN outperformed the others in terms of the I_{sp} , regardless of its chamber conditions; hence, its overall performance was the best under all the examined NPRs.

4.5. Aspiration Drag

Aspiration drag is one of the main factors affecting the performance of DBNs during the startup phase. It occurs when a low-pressure recirculation zone forms inside the nozzle, thereby reducing the wall pressure ($P_w < P_a$). The resulting pressure difference causes a reverse flow that generates a thrust opposite the nozzle face.

Aspiration drag becomes more significant when switching from sea-level to high-altitude operation, as pressure variations alter the flow separation and recirculation zones.

In this section, the aspiration drag in DBNs (including its calculation, effect on total thrust, and behaviour at mode transitions) is analysed to provide a fundamental understanding regarding the anticipation drag effects on nozzle efficiency and offer guidance for altitude adaptability with DBNs.

Following the completion of the transition phase, the recirculation zone decreased, thus causing the aspiration drag to decrease significantly.

According to Frey and Hagemann (1999), the aspiration-drag coefficient can be calculated as the ratio of F_D to F , as expressed by the following equation:

$$F_D = \int_{A_i}^{A_e} (P_a - P_w) dA \quad (10)$$

$$F_T = mV_i + (\dot{P}_i - P_a)A_i \quad (11)$$

$$F = F_T - F_D \quad (12)$$

$$C_D = \frac{F_D}{F} 100 \quad (13)$$

A_i denotes the area of the separation plane; A_e signifies the exit area of the nozzle extension; V_i and P_i represent the average velocity and pressure at the separation plane, respectively; and m signifies the mass flow rate. Moreover, viscous frictional drag was incorporated into the computation of thrust and aspiration drag (Liu & Li, 2023).

Table 5 Aspiration Drag in DBNs at Different NPRs

NPRs	TIC DBN (%)	MLN DBN (%)	TOP DBN (%)
05	11.27	18.49	27.039
10	9.535	6.00	10.95
12	17.99	5.634	8.608
20	7.862	5.18	0.874
40	2.286	0.748	0.414
50	2.473	0.366	0.285
80	0.328	0.0233	0.0309
100	0.0207	00	00
200	00	00	00

Table 5 lists the aspiration-drag values for the TIC DBN, MLN DBN, and TOP DBN designs.

DBN across different NPRs. The aspiration drag was highest at lower NPRs (NPR 5), with the TOP DBN exhibiting the greatest drag, thus indicating significant thrust loss owing to a greater pressure difference between the recirculating zones. As the NPR increased to 10–12, all designs showed reduced aspiration drag, thus reflecting the transition of the nozzle toward vacuum mode.

Notably, the TIC DBN indicated its peak aspiration drag at NPR = 12. In the mid-to-high NPR range (20–50), the aspiration drag continued to decline, thus allowing for a more effective model interpretation. This decline was particularly pronounced in the TOP DBN, which presented a higher regression rate than the TIC DBN. At NPRs of 80 and above, the aspiration drag virtually disappeared for all designs, thus signifying a transition to vacuum-mode operation, where the aspiration drag was minimal.

Among the three designs, the TOP DBN exhibited the most efficient performance, particularly during the critical transition phase. Although it indicated the highest drag during the initial aspiration at NPR = 5, the value decreased significantly as NPR increases, ultimately reaching 0.285% at NPR = 50. This reduction occurred rapidly and facilitated a smoother transition while superior thrust levels were maintained. By contrast, the TIC DBN exhibited a relatively low improvement rate, with higher drag values that remained consistent throughout the mid-range NPRs. Meanwhile, the MLN DBN showed a

continuous, albeit less pronounced, decrease in aspiration drag. Consequently, the TOP DBN is superior for minimising aspiration drag across a wide range of NPRs.

These observations align with the findings of Frey and Hagemann (1999), who reported that aspiration drag decreases as the NPR or altitude increases. The DBNs indicated a significant decrease in drag during the transition phase, as similarly observed in the CP model, in which the aspiration drag transitioned abruptly to low values in the fast mode. At NPR 100, all nozzle designs demonstrated a relatively low drag, thus indicating strong performance in the vacuum mode, as suggested by Frey and Hagemann (1999).

5. CONCLUSION

This study aimed to identify the optimal geometrical configurations that minimise performance losses and side loads while maximising altitude adaptability. Various first-bell profiles were analysed, including the TIC, TOP, and MLN profiles, which were associated with a CP expansion in the second-bell shape. The findings can provide ideas for enhancing the functionality and design possibilities of DBNs in aerospace applications.

All three DBN designs exhibited excellent adaptability to different altitudes, with each operating optimally within their respective ranges. The TIC nozzle demonstrated more aggressive shock structures at lower NPRs, whereas the TOP nozzle provided the smoothest transition and the most consistent performance within a wider altitude range. At intermediate NPRs, the MLN achieved average performance compared with the other two designs.

The flow-separation behaviour of DBNs significantly affects their overall performance. This study identified three distinct transition modes: sea-level, sneak, and high-altitude modes. Notably, the TOP nozzle exhibited a faster transition with FSS at NPR = 12 compared with the other designs.

The flow-separation behaviour of DBNs significantly affects their overall performance. This study identified three distinct transition modes: sea-level, sneak, and high-altitude modes. Notably, the TOP nozzle exhibited a faster transition with FSS at NPR = 12 compared with the other designs.

The TOP DBN consistently demonstrated the highest C_F of 707.11 under vacuum conditions, along with the highest I_{sp} of 716.78 m/s in high-altitude mode. Hence, it is the most efficient design, particularly at high altitudes where engines must convert propellants into thrust with maximum efficiency. The TOP DBN achieved the most significant reduction in aspiration drag at higher NPRs, particularly during operational transients associated with the transition stage. Despite exhibiting the highest initial drag at low NPRs, the TOP design was the most effective in minimising drag losses.

In terms of performance quality, the TOP DBN was the lightest and most optimised dual-bell configuration, thus rendering it the best option for aerospace applications that require high performance across a wide range of altitudes. It provided more rapid transitions, higher thrust

efficiency, and reduced drag, thus rendering it a superior option for future rocket-propulsion systems. These findings are critical to the design and performance of DBNs, which ultimately enable propulsion systems to operate more efficiently in aerospace applications.

In future studies, the effects of high-temperature propulsion gases on DBN design can be investigated using the method of characteristics. The incorporation of a central body into the base nozzle may mitigate FSS during sea-level operations (overexpanded conditions).

This study was based on a single-phase flow model; however, integrating combustion chamber modelling or multiphase-flow dynamics into CFD simulations can enhance our understanding of nozzle performance under various operating conditions. Future investigations should include experimental trials of the proposed nozzle configurations and compare the results with those obtained from CFD simulations, particularly regarding shock-wave behaviour and flow separation.

ACKNOWLEDGEMENTS

The authors acknowledge Chaimaa Chebane, Sofia Chehat, as well as Anas and Douha Hamaidia, for granting the time to prepare this manuscript.

CONFLICT OF INTEREST

The authors declare that they have no competing interests.

AUTHORS CONTRIBUTION

T. Chehat: conceptualization, original draft, visualization, data analysis, validation, writing and contributed to answering comments; **H. Kbab:** supervision, review and contributed to answering comments; **W. Hamaidia:** supervision, review and contributed to answering comments; **B. Benaouda Zouaoui:** review.

REFERENCES

- Cimini, M., Martelli, E., & Bernardini, M. (2021). Numerical analysis of side-load reduction in a sub-scale dual-bell rocket nozzle. *Flow, Turbulence and Combustion*, 107(3), 551-574. <https://doi.org/10.1007/s10494-021-00243-4>
- Davis, K., Fortner, E., Heard, M., McCallum, H., & Putzke, H. (2015). *Experimental and computational investigation of a dual-bell nozzle*. 53rd AIAA Aerospace Sciences Meeting (p. 0377). <https://doi.org/10.2514/6.2015-0377>
- Fluent, A. N. S. Y. S. (2021). *Ansys fluent theory guide*. ANSYS, Inc. and Ansys Europe, Ltd. Are UL Registered ISO 9001: 2015
- Frey, M., & Hagemann, G. (1999). Critical assessment of dual-bell nozzles. *Journal of Propulsion and Power*, 15(1), 137-143. <https://doi.org/10.2514/2.5402>

- Génin, C., Gernoth, A., & Stark, R. (2013a). Experimental and numerical study of heat flux in dual bell nozzles. *Journal of Propulsion and Power*, 29(1), 21-26. <https://doi.org/10.2514/1.B34479>
- Génin, C., Stark, R. H., & Schneider, D. (2013b). *Transitional behavior of dual bell nozzles: contour optimization*. 49th AIAA/ASME/SAE/ASEE Joint Propulsion Conference (p. 3841). <https://doi.org/10.2514/6.2015-0377>
- Génin, C., Stark, R., Haidn, O., Quring, K., & Frey, M. (2013c). Experimental and numerical study of dual bell nozzle flow. *Progress in Flight Physics*, 5, 363-376. <https://doi.org/10.1051/eucass/201305363>
- Génin, C., Stark, R., Karl, S., & Schneider, D. (2012, July). *Numerical investigation of dual bell nozzle flow field*. 48th AIAA/ASME/SAE/ASEE Joint Propulsion Conference & Exhibit (p. 4164). <https://doi.org/10.2514/6.2012-4164>
- Hagemann, G., Immich, H., Van Nguyen, T., & Dumnov, G. E. (1998). Advanced rocket nozzles. *Journal of Propulsion and Power*, 14(5), 620-634. <https://doi.org/10.2514/2.5354>
- Hagemann, G., Terhardt, M., Haeseler, D., & Frey, M. (2002). Experimental and analytical design verification of the dual-bell concept. *Journal of Propulsion and Power*, 18(1), 116-122. <https://doi.org/10.2514/2.5905>
- Hamaidia, W., Zebbiche, T., Sellam, M., & Allali, A. (2019). Performance improvement of supersonic nozzles design using a high-temperature model. *Proceedings of the Institution of Mechanical Engineers, Part G: Journal of Aerospace Engineering*, 233(13), 4895-4910. <https://doi.org/10.1177/0954410019831862>
- Hamitouche, T., Sellam, M., Kbab, H., & Bergheul, S. (2019). Design and wall Fluid parameters evaluation of the dual-bell Nozzle. *International Journal of Engineering Research and Technology*, 12(7), 1064-1074.
- Horn, M., & Fisher, S. (1993). *Dual-bell altitude compensating nozzles*. Pennsylvania State Univ., NASA Propulsion Engineering Research Center, Volume 2.
- Kbab, H., Sellam, M., Hamitouche, T., Bergheul, S., & Lagab, L. (2017). Design and performance evaluation of a dual bell nozzle. *Acta Astronautica*, 130, 52-59. <https://doi.org/10.1016/j.actaastro.2016.10.015>
- Khare, S., & Saha, U. K. (2021). Rocket nozzles: 75 years of research and development. *Sādhanā*, 46(2), 76. <https://doi.org/10.1007/s12046-021-01584-6>
- Léger, L., Zmijanovic, V., Sellam, M., & Chpoun, A. (2020). Controlled flow regime transition in a dual bell nozzle by secondary radial injection. *Experiments in Fluids*, 61, 1-15. <https://doi.org/10.1007/s00348-020-03086-3>
- Léger, L., Zmijanovic, V., Sellam, M., & Chpoun, A. (2021). Experimental investigation of forced flow regime transition in a dual bell nozzle by secondary fluidic injection. *International Journal of Heat and Fluid Flow*, 89, 108818. <https://doi.org/10.1016/j.ijheatfluidflow.2021.108818>
- Liu, Y., & Li, P. (2023). Analysis of the aspiration drag in dual-bell nozzles. *International Journal of Aeronautical and Space Sciences*, 24(2), 467-474. <https://doi.org/10.1007/s42405-022-00541-9>
- Martelli, E., Nasuti, F., & Onofri, M. (2007). Numerical parametric analysis of dual-bell nozzle flows. *AIAA journal*, 45(3), 640-650. <https://doi.org/10.2514/1.26690>
- Nürnberg-Génin, C., & Stark, R. (2010). Experimental study on flow transition in dual bell nozzles. *Journal of Propulsion and Power*, 26(3), 497-502. <https://doi.org/10.2514/1.47282>
- Östlund, J. (2002). *Flow processes in rocket engine nozzles with focus on flow separation and side-loads* [Doctoral dissertation, Mekanik].
- Scharnowski, S., & Kähler, C. J. (2021). Investigation of the base flow of a generic space launcher with dual-bell nozzle. *CEAS Space Journal*, 13(2), 197-216. <https://doi.org/10.1007/s12567-020-00333-5>
- Schneider, D., & Génin, C. (2016). Numerical investigation of flow transition behavior in cold flow dual-bell rocket nozzles. *Journal of Propulsion and Power*, 32(5), 1212-1219. <https://doi.org/10.2514/1.B36010>
- Stark, R., & Nürnberg-Génin, C. (2010, July). *Side loads in dual bell nozzles, part i: Phenomenology*. 46th AIAA/ASME/SAE/ASEE Joint Propulsion Conference & Exhibit (p. 6729). <https://doi.org/10.2514/6.2010-6729>
- Stark, R., Génin, C., Mader, C., Maier, D., Schneider, D., & Wohlhüter, M. (2019). Design of a film-cooled dual-bell nozzle. *Acta Astronautica*, 158, 342-350. <https://doi.org/10.1016/j.actaastro.2018.05.056>
- Stark, R., Génin, C., Schneider, D., & Fromm, C. (2016). Ariane 5 performance optimization using dual-bell nozzle extension. *Journal of Spacecraft and Rockets*, 53(4), 743-750. <https://doi.org/10.2514/1.A33363>
- Toufik, H., Mohamed, S., Hakim, K., Saïd, B., & Lynda, L. (2016, March). *Design and performance of the dual-bell nozzle*. 2016 IEEE Aerospace Conference (pp. 1-7). IEEE. <https://doi.org/10.1109/AERO.2016.7500518>
- Verma, M., Arya, N., & De, A. (2020). Investigation of flow characteristics inside a dual bell nozzle with and without film cooling. *Aerospace Science and Technology*, 99, 105741. <https://doi.org/10.1016/j.ast.2020.105741>
- Verma, S. B., Hadjadj, A., & Haidn, O. (2015). Unsteady flow conditions during the dual-bell sneak transition. *Journal of Propulsion and Power*, 31(4), 1175-1183. <https://doi.org/10.2514/1.B35558>

- Verma, S. B., Stark, R., & Haidn, O. (2013). Reynolds number influence on dual-bell transition phenomena. *Journal of Propulsion and Power*, 29(3), 602-609. <https://doi.org/10.2514/1.B34734>
- Verma, S. B., Stark, R., & Haidn, O. (2014). Effect of ambient pressure fluctuations on dual-bell transition behavior. *Journal of Propulsion and Power*, 30(5), 1192-1198. <https://doi.org/10.2514/1.B35067>
- Verma, S. B., Stark, R., Nuerenberger-Genin, C., & Haidn, O. (2010). Cold-gas experiments to study the flow separation characteristics of a dual-bell nozzle during its transition modes. *Shock Waves*, 20, 191-203. <https://doi.org/10.1007/s00193-010-0259-x>
- Wu, K., Sohn, G. C., Deng, R., Jia, H., Kim, H. D., & Su, X. (2023). Study on wall pressure and hysteresis behaviors of a novel dual-bell nozzle. *Journal of Mechanical Science and Technology*, 37(9), 4639-4646. <https://doi.org/10.1007/s12206-023-0819-5>
- Yazhou, L. I. U., Ping, L. I., Hongyu, C. H. E. N., Jianwen, Y. A. N. G., & Yidan, C. H. E. N. (2022). Design of dual-bell nozzles with different extension pressure distributions. 37(2), 424-432. <https://doi.org/10.13224/j.cnki.jasp.20210096>